Activated Functionalized Carbon Nanotubes and 2D Nanostructured MoS₂ Hybrid Electrode Material for High-Performance Supercapacitor Applications

Honey Gupta, Sagar Mothkuri, Ruairi McGlynn, Darragh Carolan, Paul Maguire, Davide Mariotti, P. K. Jain, Tata Narasinga Rao, G. Padmanabham, and Supriya Chakrabarti*

Alkali-activated functionalized carbon nanotubes (AFCNTs) and 2D nanostructured MoS₂ are investigated as a novel hybrid material for energy-storage applications. The nanoflower-like 2D MoS₂ is grown on the surface of AFCNT using the controlled one-step hydrothermal technique. The activation of functionalized carbon nanotubes results in greater performance due to the improved surface area. The Brunauer–Emmett–Teller (BET) surface area of the AFCNTs is found to be 594.7 m² g⁻¹ which is almost 30 times of the as-prepared carbon nanotubes (CNTs). The improved surface area with attached hydroxyl and carboxylic functional groups helps in the attachment of MoS₂ nanoflowers onto the AFCNT, thus reducing the interfacial resistance and providing an easy path for electron transfer. The electrochemical analysis shows a high specific capacitance of 516 F g⁻¹ at 0.5 A g⁻¹ with a corresponding energy density of 71.76 Wh kg⁻¹, which is an encouraging reported value from AFCNT and MoS₂ hybrid material. To the best of our knowledge, herein, the first report on AFCNTs and 2D MoS₂ nanostructured hybrid electrode material for supercapacitor applications is provided, and promising results in terms of specific capacitance, energy density, and power density by boosting the properties of individual material are explained.

H. Gupta, S. Mothkuri, P. K. Jain, T. N. Rao, G. Padmanabham, S. Chakrabarti
Centre for Carbon Materials
International Advanced Research Centre for Powder Metallurgy and New Materials
P.O. Balapur, Hyderabad 500005, Telangana, India
E-mail: supriyac79@gmail.com

R. McGlynn, D. Carolan, P. Maguire, D. Mariotti, S. Chakrabarti
Nanotechnology & Integrated Bio-Engineering Centre (NIBEC)
School of Engineering
Ulster University
Jordanstown, Co. Antrim, Newtownabbey BT37 0QB, UK
E-mail: s.chakrabarti@ulster.ac.uk

The ORCID identification number(s) for the author(s) of this article can be found under https://doi.org/10.1002/pssa.201900855.

1. Introduction

The rampant use of fossil fuels is adversely affecting the environment and eventually increasing pollution which essentially triggered researchers for finding efficient energy-storage devices.[1] The increasing demand for power and energy turned the recent research trends toward the development of more efficient electrode materials for energy-storage devices.

Supercapacitors (SCs), as energy-storage devices, are under substantial attention due to negligible environmental concerns, low costs, ease of device fabrication, portable nature, higher power and energy densities, fast charge/discharge capabilities, and excellent cyclic stabilities.[2–10] The electrode material plays the most important role in the charge storage performance of the SC; therefore, the potential research is focused on developing different electrode materials for efficient energy storage.

Depending on the charge storage mechanism, the SCs can be categorized as electric double-layer capacitors (EDLCs), pseudocapacitors, and hybrid capacitors. The EDLC materials are typically high-surface-area (>1000 m² g⁻¹) nanoporous carbon-based materials and possess high electrical conductivity,[11–13] such as activated carbon,[14] graphene,[15,16] and carbon nanotubes (CNTs).[17] The charge transfer in EDLCs is a non-Faradic process; therefore, the interface between the electrode and the electrolyte is utilized to store the charge, whereas, in the pseudocapacitors, the charge transfer mechanism is Faradic under which fast reversible redox reactions occur at the electrode surface. A series of materials used as pseudocapacitives are potentially metal oxides,[18,19] metal hydroxides,[20,21] and metal sulfides.[22,23]

Carbon-based electrodes such as CNTs have a high surface area, controlled morphology, surface functionality, and excellent electrical conductivity that make CNTs promising candidates, but poor energy storage capacity restricts them for use in practical applications.[24] Transition metal oxides are the promising materials due to the multiple oxidation states which change at different potentials and hence, enhance the capacitance value.[25]

ADVANCED
SCIENCE NEWS
www.advancedsciencenews.com

pss a
physica status solidi
www.pss-a.com

A myriads of metal oxides such as RuO_2,[26,27] IrO_2,[28] MnO_2,[29] NiO,[30,31] Co_2O_3,[32] Sno_2,[33] V_2O_5,[34] and MoO_x,[35] has been researched. MnO_2 and RuO_2 are the widely investigated pseudo-capacitive materials[36] among other metal oxides. RuO_2 is found to be a good electrode material because of its multiple oxidation state and good reversibility, but the cost and rare availability restrict its commercial applications.[37,38]

Recent studies show that the layered transition-metal dichalcogenides family has proven to be the ideal choice for the electrode material because of their excellent electrical, mechanical, chemical, and thermal proprieties.[39] Therefore WS_2, VS_2, SnS_2, and MoS_2 have been further investigated.[40–42]

Although several pseudocapacitive dichalcogenides have been studied, however, MoS_2 nanostructure was found to be a promising 2D material for the SC application. MoS_2 is the first transition-metal dichalcogenides to be used in Li-ion batteries as electrode materials; hence, it is a high-energy and high-current-density electrode material.[43] MoS_2 possesses many advantageous merits such as a high intrinsic ionic conductivity,[44] a 2D layered structure same as graphene, which provides a high surface area for charge storage, and a higher theoretical capacity than graphite.[45] The charge storage in MoS_2 nanostructures occurs via the diffusion of ions into the interlayer or double-layer charging on the external surface.[46–48] MoS_2 has excellent redox properties which help in ion diffusion at the layer interfaces during the charge transfer reaction.[49,50] In contrast, MoS_2 alone has a lower capacitance and a poor cyclic stability resulting from low electrical conductivity.[45]

Therefore, this research is utterly focused on designing hybrid with alkali-activated functionalized carbon nanotubes (AFCNTs) and MoS_2 nanostructures to address the issue with CNT and MoS_2. In this study, using a simple hydrothermal approach, MoS_2 nanoflowers were grown on the surface of AFCNTs, which

helps in achieving a minimum charge transfer resistance. It also helps in preventing the agglomeration during charge–discharge cycles and acquiring the capacitive behavior of both EDLC and pseudo-types which ultimately enhance the net specific capacitance value. The alkali activation of CNTs has been done to enhance the electrochemically active surface area and finally the AFCNT-MoS_2 hybrid electrode material furnished, encouraging supercapacitive properties. There are several reports on 2D MoS_2 alone and their hybrid materials, but in our recent work, the introduction of AFCNTs into MoS_2 boosted the specific capacitance value to the $516\,F\,g^{-1}$ at a current density of $0.5\,A\,g^{-1}$, which is, utmost, reported as of now. The corresponding energy density and power density are $71.76\,Wh\,kg^{-1}$ and $1000\,W\,kg^{-1}$, respectively.

2. Results and Discussion

2.1. Structural and Chemical Analyses

In this work, the MoS_2 nanostructure and AFCNT-MoS_2 hybrid material were successfully synthesized using the facile hydrothermal method. The crystallinity of the nanostructured material was confirmed by X-ray diffraction (XRD). The XRD patterns of the as-synthesized MoS_2 and AFCNT-MoS_2 (**Figure 1**a) were well synchronized in their diffraction angles and are in good agreement with standard JCPDS 37-1492 data.

The XRD pattern of MoS_2 shows diffraction peaks at $2\theta = 14.3°$, $33.7°$, $39.8°$, and $59.1°$, which correspond to (002), (101), (103), and (110) planes of the hexagonal MoS_2 phase, respectively, with lattice constants $a = b = 3.161\,Å$ and $c = 12.299\,Å$ (JCPDS 37-1492). The presence of the strong diffraction peak at (002) plane explains that the stacking of MoS_2 layers takes place along the C axis.[51] The XRD pattern of
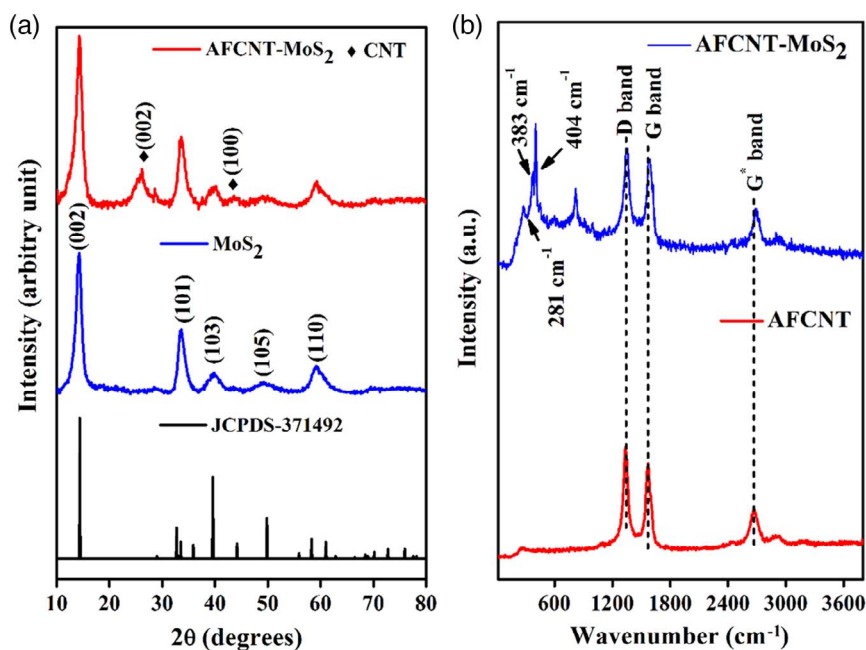

Figure 1. a) XRD pattern of AFCNT-MoS_2, MoS_2, and the stick pattern at the bottom is the standard JCPDS data (card no. 37-1492) corresponding to the hexagonal crystalline phase of the MoS_2, b) Raman spectra of AFCNT and AFCNT-MoS_2.

$AFCNT-MoS_2$ hybrid clearly indicates the presence of MoS_2 peaks as well as the diffraction peaks corresponding to CNT.

The diffraction peaks at $2\theta = 26.3°$ and $43.5°$ correspond to the (002) and (100) reflection planes of CNTs which indicate the presence of the CNTs in the hybrid material. However, it is shown in Figure 1a that the intensity of the major diffraction peaks of CNT was suppressed due to the MoS_2 nanoflowers densely covered on the surface of CNTs.[24] The XRD spectrum of CNTs, functionalized carbon nanotube (FCNTs), and AFCNTs is shown in Figure S1, Supporting Information.

The d-spacing value from Figure S2, Supporting Information was calculated for the broad d_{002} peak, using Bragg's law. The d-spacings for d_{002} peak of FCNTs and AFCNTs were found to be 0.3432 and 0.3438 nm, respectively. This slight change of d-spacing at a higher value indicates the insertion of potassium (K) during the time of the activation process.[52] The d-spacing (the value obtained from the XRD pattern of MoS_2) was 0.62 nm for (002) diffraction plane of MoS_2, which is in agreement with the transmission electron microscopy (TEM) results (**Figure 2**d).

The d-spacing was calculated for the (002) plane of MoS_2 and (002) plane of CNT in the XRD spectrum of the $AFCNT-MoS_2$ hybrid. In the XRD of MoS_2, the position of (002) plane was at $14.18°$ and in the $AFCNT-MoS_2$ hybrid, it was found to be at $14.23°$. This shifting of planes from $14.18°$ to $14.23°$ can be attributed to decrement in the interlayer distance from 6.24 to 6.21 nm, respectively. This could be explained by the incorporation of the AFCNT into the MoS_2 during $AFCNT-MoS_2$ formation.[53]

Further, Raman spectroscopy was used to investigate the growth mechanism of $AFCNT-MoS_2$ hybrid, which is shown in Figure 1b. The Raman spectrum of AFCNT in Figure 1b shows the D band at $1351\,cm^{-1}$ that arises from disordered carbon or defective carbon sites in the structure of AFCNT and G band at $1589\,cm^{-1}$ which represents the E_{2g} zone center mode of the crystalline graphite and it also represents the graphitic nature present.[54,55] The Raman spectrum of $AFCNT-MoS_2$ hybrid indicates the Raman bands corresponding to MoS_2 as well as CNTs. The bands observed at $383\,cm^{-1}$ and $404\,cm^{-1}$ correspond to the E_{2g} and A_{1g} modes of hexagonal MoS_2, respectively.[56] The Raman analysis of $AFCNT-MoS_2$ hybrid confirms the presence of both the materials AFCNTs and MoS_2.

Fourier infrared transform spectroscopy (FTIR) analysis has been used further to investigate the functional group attached on the surface of CNTs after the functionalization process shown in Figure S3, Supporting Information. The intense peak at $3435.22\,cm^{-1}$ refers to the O—H stretching vibrations of hydroxyl and carboxyl groups. The three other major peaks found in the FTIR spectrum are 1628.61, 1380.85, and $1101.10\,cm^{-1}$, corresponding to C=C, —OH, and C—O functional groups, respectively. The other two minor peaks at 2917.57 and $2845.97\,cm^{-1}$ belong to C—H bonding of carboxyl group and might arise from the traces of water in the KBr disk used for the analysis. The peak in the fingerprint region at $604.97\,cm^{-1}$ represents a bending vibration of CH bond vibrations, indicating the surface functionalization of CNTs by the carboxylic group. The overall results indicate that the CNTs were properly functionalized.[56,57]

To gain further insights into the chemical nature and bonding state of MoS_2 nanoflowers deposited on the AFCNT surface, the hybrid was characterized using X-ray photoelectron spectroscopy (XPS). The survey scan shown in **Figure 3**a indicates the presence of main elements Mo, S, C, and O of the $AFCNT/MoS_2$ hybrid material. The atomic percentage ratio of Mo and S was found to be 1:1.72 from the XPS survey scan. This stoichiometric ratio (1:1.72) of Mo to S from XPS spectra suggests a structure close to MoS_2. Researchers have reported a similar kind of slight variation in the stoichiometric ratio of MoS_2 obtained from the XPS spectra.[58–61]

This slight variation in the stoichiometric ratio could be due to the constrained growth of MoS_2 on the surface of AFCNT, as well some Mo is present as an oxide or sulfate in the hybrid sample.

This could be due to the constrained growth of MoS_2 on the surface of AFCNT, as well some Mo is present as an oxide or sulfate in the hybrid sample. In Figure 3a, C 1s peak may relate to the graphite-like sp^2-hybridized carbon and O 1s for the functional groups such as —COOH, —CO, etc.

The high-resolution XPS spectra of Mo 3d, S 2p, and C 1s regions are shown in Figure 3b–d, respectively. The deconvolution of the high-resolution Mo 3d spectrum in Figure 3b shows peaks at 226.90, 229.38, 232.53, 233.00, and 236.15 eV. The peak at 226.90 eV corresponds to the S 2s binding energy of MoS_2 and the deconvoluted peaks at 229.38 and 232.53 eV correspond to Mo $3d_{5/2}$ and Mo $3d_{3/2}$ of the 2H phase of MoS_2. These peaks represent the presence of Mo^{4+} oxidation state.[62] The other two peaks at 233.00 and 236.15 eV correspond to the slight formation of molybdenum oxide[63] and oxidized molybdenum
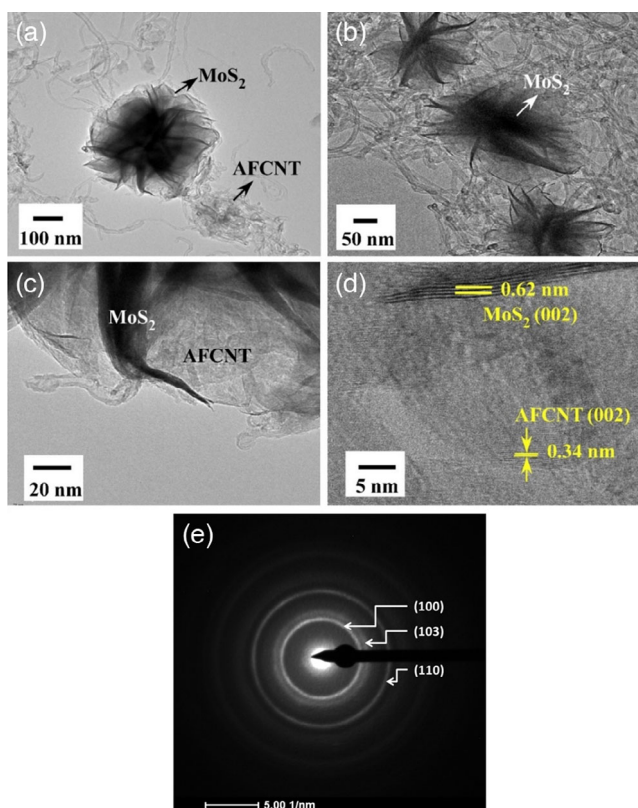

Figure 2. a–c) TEM image of $AFCNT-MoS_2$ hybrid, d) high-resolution TEM image of $AFCNT-MoS_2$ hybrid, and e) SAED pattern of $AFCNT-MoS_2$ hybrid.
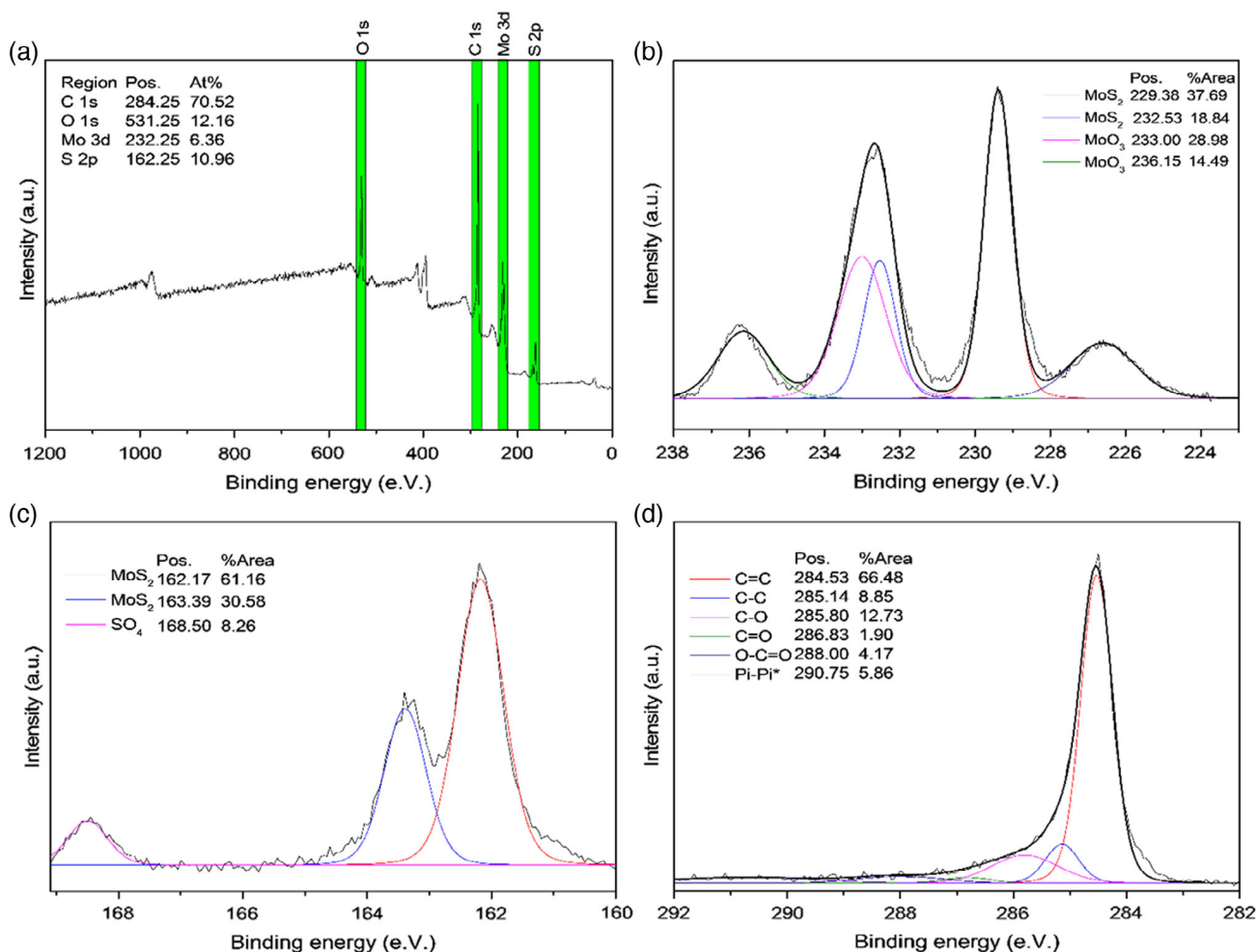
Figure 3. a) XPS survey spectrum of AFCNT-MoS$_2$ hybrid and high-resolution spectra of b) Mo 3d, c) S 2p, and d) C 1s peaks.

forms of MoO$_3$ and MoO$_4^{2-}$ which are generally present in the samples.[64]

The S 2p spectrum (Figure 3c) indicates two doublets such as S 2p$_{5/2}$ and S 2p$_{3/2}$ of MoS$_2$ at 162.17 and 163.39 eV.

The XPS spectrum for C 1s exhibits the main peak at 284.53 eV (Figure 3d), and it relates to the graphite-like sp^2-hybridized carbon atom.[65] This main peak position at 284.53 eV of C 1s indicates that there is no significant change in the chemical state of carbon atoms after MoS$_2$ loading on AFCNT. The deconvolution of C 1s spectrum shows that it contains a large amount of C—O species (285.80 eV), and the other peaks are C=C, C—C, C=O, and O—C=O corresponding to 284.53, 285.14, 286.83, and 288 eV, respectively. The presence of oxygen-bounded C atoms is due to the nitric acid-treated CNT surface with a number of oxygen-containing functional groups.

2.2. Microstructural Analysis

It is shown in **Figure 4**a that MoS$_2$ exist as spherical nanoflowers with very closely spaced petals. Higher magnification images

shown in Figure 4b reveal that the MoS$_2$ nanoflowers are closely packed with CNT distributed as spaghetti-like structures. The petals of the nanoflowers consist of several layers with tiny spacings in between, which help in the incorporation of the positive electrolyte ion (K$^+$) during the redox reactions. In this hybrid nanostructure, AFCNT acts as the current-carrying support, whereas MoS$_2$ participates in the majority of charge–discharge reactions.

Activation energy plays a key role in the growth of hybrid nanostructures. The high surface area of AFCNT decreases the activation energy required for the nucleation of MoS$_2$, it subsides the complete growth of MoS$_2$ nanoflowers. Henceforth, the size of MoS$_2$ reduced prominently after composite formation.[66,67] Liu et al.[67] also reported the reduction in stacking and yield in the growth of MoS$_2$ nanosheets after composites with CNTs and mostly monolayer and bilayer formations of MoS$_2$ were observed.

Although it appears as if the AFCNTs are distributed over the surface of MoS$_2$, the actual growth mechanism shows that the surface of AFCNT acts as the nucleation site for the growth of MoS$_2$ nanoflowers. This growth mechanism is visually well established from the TEM analysis of Figure 2.
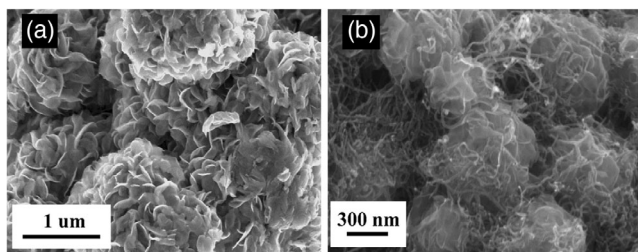
Figure 4. FESEM images of a) MoS_2 and b) $AFCNT-MoS_2$.

From the TEM images, it is clear that MoS_2 nanoflowers were grown on the AFCNT surface, same observations were also confirmed from field-emission scanning electron microscopy (FESEM) (Figure 4) results. It was found that there are plenty of nanoflakes with several nanometer thickness, which ultimately constructs the flower-like morphology on the surface of the AFCNTs (Figure 2b,c). This observation was further corroborated from the high-resolution transmission electron microscopy (HRTEM) (Figure 2d) image in which the MoS_2 is clearly distributed on the surface of AFCNT. Figure 2e shows the selected-area electron diffraction pattern (SAED) for $AFCNT-MoS_2$ which clearly indicates the crystalline feature of MoS_2. The SAED pattern (Figure 2e) reveals several rings, which are indexed as the (100), (103), and (110) of MoS_2, respectively, demonstrating the presence of crystalline MoS_2 in the hybrid. It confirmed that both MoS_2 and AFCNT retained their crystalline features after the hybrid synthesis which further supports the XRD analysis (Figure 1a). From the HRTEM images of $AFCNT-MoS_2$ shown in Figure 2d, it is evident that the lattice fringes of AFCNT and MoS_2 overlap each other with MoS_2 lattice fringes popping up, showing that MoS_2 is grown over the surface of AFCNTs. A lattice spacing of 0.62 nm was evaluated for MoS_2 lattice fringes (Figure 2d), and it was found to be in a good match with the calculated d-spacing value from the XRD pattern of hexagonal MoS_2.

The specific surface area measurement of CNT and AFCNT was determined by Brunauer–Emmett–Teller (BET) analyses. As shown in Figure S11, Supporting Information, the obtained N_2 adsorption–desorption isotherms of CNT and AFCNT are typical type IV, according to the International Union of Pure and Applied Chemistry (IUPAC) classification. These results suggest the presence of mesoporosity in the samples and slit-size pores, which is the typical characteristic of type IV isotherms. As shown in Figure S11, Supporting Information, the CNT isotherm has a low uptake of the physiosorbed volume below the partial pressure of 0.5, which indicates the presence of micropore volume that is negligible in the sample. However, at a relative pressure higher than 0.7, there is an appearance of the H3 hysteresis loop. The typical isotherm of AFCNT also shows type IV behavior with a prominent hysteresis loop.[52] Mesoporosity comes from the central canal and entanglement of CNTs.[52] The alkali activation process is the key factor to gain mesoporosity to increase the effective surface area in the nanotubes. Here, the activation of CNTs was conducted with KOH, because it is more efficient in providing the mesoporosity to the CNTs, as shown in the isotherm of AFCNT.[52] From Figure S11, Supporting Information,

it is clearly evident that after KOH activation there is an increase in N_2 uptake at a low partial pressure, as compared with the nonactivated CNT. The increment in N_2 uptake of the AFCNT sample at a low partial pressure also confirms the generation of micropores. As shown in Figure S11, Supporting Information, the more pronounced shape of hysteresis can be seen in the AFCNT isotherm which confirms the wider distribution of mesopore size. The KOH activation process helped in making the nanotube structure more porous, which eventually increased the surface reactivity and surface area in AFCNT. This increased surface area is due to the generation of both micropores and mesopores in the sample.

The BET surface area was calculated from the quantity of the monolayer of nitrogen gas adsorbed on the surface of CNT and AFCNT samples. BET surface areas for the CNT and AFCNT hybrids were found to be 20 and 594.7 $m^2\,g^{-1}$. Around 30 times enhancement in the specific surface area was achieved by the alkali activation process of the FCNT, which finally boosted the specific surface area of $AFCNT-MoS_2$ hybrid compared with $FCNT-MoS_2$. The introduction of AFCNT in the hybrid played the vital role in the improvement of the capacitive performance value due to the enhanced surface area. In addition AFCNT worked as an easy condcuting path for electron transfer in the SC.

2.3. Electrochemical Studies of the Hybrid Nanostructured Material

Figure 5 shows the electrochemical performances of FCNT, AFCNT, MoS_2, $FCNT-MoS_2$, and $AFCNT-MoS_2$ electrodes in a two-electrode system. The electrochemical performance of the as-synthesized FCNT, AFCNT, MoS_2, $FCNT-MoS_2$, and $AFCNT-MoS_2$ hybrid nanostructured material was investigated using the two-electrode electrochemical cell in 3 M KOH solution as an electrolyte. From Figure 5a, it is shown that only carbon-based materials exhibit quasirectangular curves typical to EDLC, the other materials as MoS_2, $FCNT-MoS_2$, and $AFCNT-MoS_2$ are observed to undergo redox reactions. These statements are in excellent agreement, close to the ideal characteristics of the materials, and hence prove the synthesis of materials is excellent. The redox peaks (multiple oxidation peaks) in $AFCNT-MoS_2$ can be observed clearly and have taken up the wider area when compared with $FCNT-MoS_2$ (Figure 5a). The wider area can be attributed to the enhanced ability of MoS_2, when synthesized along with activated FCNT. The activated FCNT provides additional surface area[68–70] for the electrolyte in addition to MoS_2 enhancing the overall surface. The enhanced surface area thus widens up the area under the cyclic voltammetry (CV) curve and increases the specific capacitance value for the same scan rate, as discussed later. The effect of activation is also seen in terms of the specific capacitance from Figure 5c.

A similar trend is observed in galvanostatic charge–discharge (GCD) in terms of the specific capacitance (Figure 5b). The discharge time of the pseudo- (MoS_2) and hybrid ($FCNT-MoS_2$ and $AFCNT-MoS_2$) materials is higher than that of the carbon-based materials (EDLCs). It is due to the redox mechanism involved in the former two types of materials.[56] It can also be observed that the charge–discharge profiles (Figure 5b) are observed to be linear in the case of FCNT and AFCNT, and nonlinearity in the
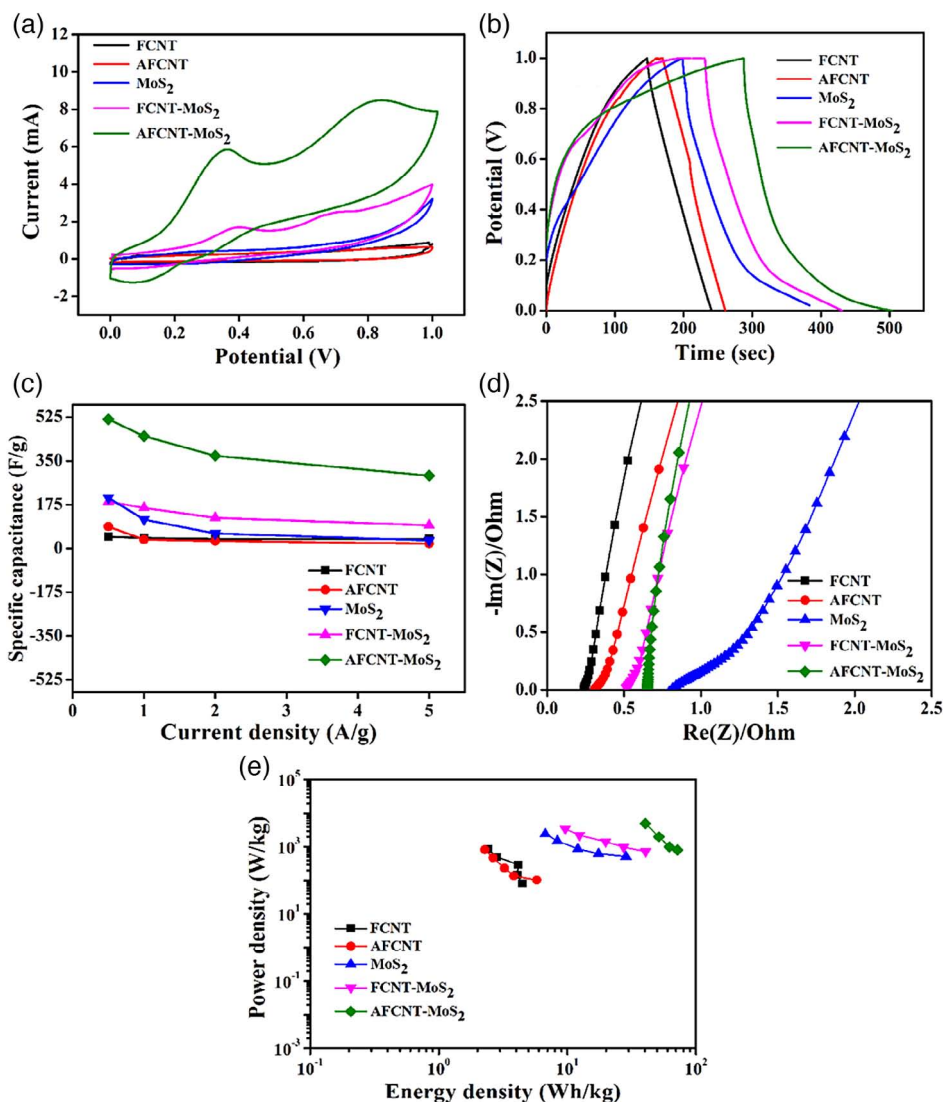
Figure 5. Electrochemical performances of FCNT, AFCNT, MoS$_2$, FCNT-MoS$_2$, and AFCNT-MoS$_2$ electrodes in a two-electrode system: a) CV curves at a scan rate of 5 mV s^{-1}. b) GCD curves at a current density of 0.5 A g^{-1}, c) performance curves of FCNT, AFCNT, MoS$_2$, FCNT-MoS$_2$, and AFCNT-MoS$_2$ at current densities of 0.5, 1, 2 and 5 A g^{-1}. d) Nyquist plot at the low-frequency region. e) Ragone plot (energy density vs power density).

rest of the materials shows that in the latter type, the redox reactions are responsible for the nonlinear nature of the curves.[71]

As shown in Figure 5c, the specific capacitance values due to the AFCNT and MoS$_2$ nanoflower alone are 87 and 186 F g^{-1} at 0.5 A g^{-1} current density, which are quite low. The hybrid AFCNT-MoS$_2$ shows the drastic increase in the specific capacitance value which is close to the 516 F g^{-1} and maintains excellent retention even at higher current densities. The Cs (specific capacitance) values were calculated from the GCD curves using Equation (4) (S5, Supporting Information).

The specific capacitances for the materials such as AFCNT-MoS$_2$, FCNT-MoS$_2$, MoS$_2$, AFCNT, and FCNT were found to be 516, 202, 186, 87, and 46 F g^{-1} at a current density of 0.5 A g^{-1}. These values indicate that the supercapacitive performance of AFCNT-MoS$_2$ hybrid electrode is much better compared with the individual counterparts.

The electrochemical impedance spectroscopy (EIS) analysis was used to calculate the equivalent series resistance (ESR) of the material shown in Figure 5d. It can be observed that the ESR values of FCNT (0.246 Ω) and AFCNT (0.308 Ω) are smaller than all the other materials under consideration. It is due to the reaction mechanism involved, i.e., only non-Faradic reactions. However MoS$_2$ is observed to have the largest ESR value (0.672 Ω), which is a clear indication that the material is less conductive than all the other materials. Considering the hybrid nanostructures (for FCNT-MoS$_2$—0.604 Ω and AFCNT-MoS$_2$—0.6528 Ω), the ESR value is lesser than MoS$_2$, which clearly shows that the conductivity is improved by the addition of CNTs to MoS$_2$. The energy density of the material is an essential factor in terms of energy-storage capability. It is shown from Figure 5e that AFCNT-MoS$_2$ with an energy density value of 71.76 Wh kg^{-1} clearly out performs the other materials under

consideration. The improved energy density can be achieved using hybrid material by coupling activated FCNTs with MoS_2 which is a layered-structure and hence capable of storing a high number of ions during the charging phase.

The CV curves of the as-synthesized AFCNT-MoS_2 hybrid at various scan rates are shown in **Figure 6**a. The electrochemical performances curves from the CV and GCD for FCNT, AFCNT, MoS_2, and FCNT-MoS_2 are shown in Figure S6–S9, Supporting Information. From Figure 6a, it is evident that all the CV curves exhibit the same kind of shape and intense redox peaks at a particular potential. The redox peaks indicate that the specific capacitance is attributed to the electrochemical redox reactions occurring because of MoS_2, which is quite different from the electric double-layer capacitance.

The charge–discharge profile of AFCNT-MoS_2 hybrid at different current densities of 0.5, 1, 2, and $5\,A\,g^{-1}$ is shown in Figure 6b. It is quite clear from Figure 6c that as the current density increases from a lower to a higher value, the specific capacitance value decreases. As the current density increased from 0.5 to $5\,A\,g^{-1}$, the value of specific capacitance decreased from 516 to $291\,F\,g^{-1}$. The similar trend has been observed from the CV. The possible reason for the decreasing capacitance is that as the scan rate and current density increase, there is no sufficient time available for adsorption and ion diffusion inside the small pores.[12,72] The performance of SC can be understood by evaluating the cycle efficiency of the device, which is the ratio between the energy delivered and energy supplied during a particular cycle. In case of the hybrid SC due to the nonlinearity of

cell potential, Coulombic efficiency (ratio of discharge/charge durations) is overestimated; thus, reporting only Coulombic efficiency is misleading.[73] Herein, we have reported energy efficiency (the ratio of areas in discharge/charge curves, multiplied by current) in parallel with Coulombic efficiency (Figure 6d) for a more realistic characterization.

The energy in a storage device can be calculated by the integration of the GCD plot which is proportional to the area under the GCD curve. Here, from the GCD plot (Figure 6b) for each current density, we have performed the integral operation of the area under the curve for the charging part and discharging part. Finally, the percentage of energy recovered (energy efficiency) was calculated using the following equation

$$\text{Energy efficiency} = (\text{area under the discharging curve}/\text{area under the charging curve})\%$$

Figure 6d shows the comparison plot of Coulombic efficiency and energy efficiency (percentage of energy recovered) at different current densities. About 42% of energy efficiency was achieved at a current density of $5\,A\,g^{-1}$ which is an encouraging value that indicates the possibility of this hybrid electrode material in practical applications. The introduction of AFCNT in the hybrid material (Figure 6c) shows the synergistic effect in the specific capacitance value, which could be due to the combined effect of activated functionalized carbon nanotubes (EDLC) and 2D MoS_2 (pseudocapacitive).
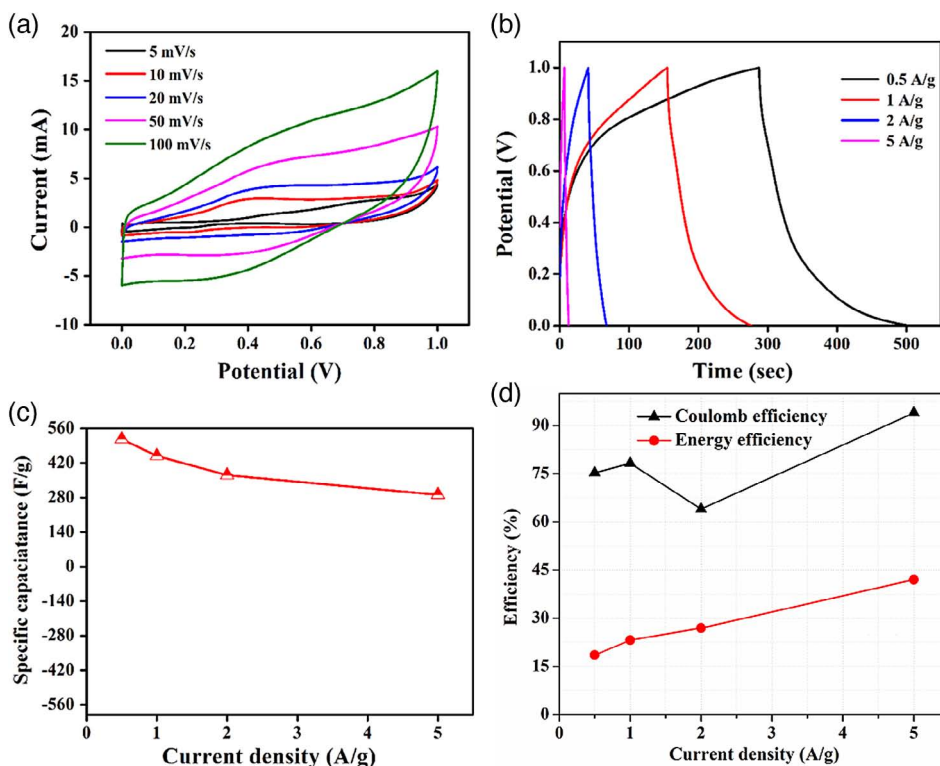

Figure 6. Electrochemical performances of the AFCNT-MoS_2 hybrid nanostructured electrode in a two-electrode system: a) CV curves at different scan rates of 5, 10, 20, 50, and $100\,mV\,s^{-1}$. b) GCD curves at different current densities of 0.5, 1, 2, and $5\,A\,g^{-1}$. c) Performance curve from GCD (current density vs specific capacitance) and d) the comparison plot of Coulombic efficiency and energy efficiency.

The introduction of the AFCNT in the MoS₂ controls the growth of MoS₂ nanoflowers which is evident from the FESEM (Figure 4b) and HRTEM (Figure 2) results, which helps in increasing the redox reaction sites and decreases the ion-transport resistance.[74] The tubular structure of AFCNT and the layered structure of MoS₂ provide the higher electrochemically active surface area which ultimately increases the specific capacitance. The cell performance of the hybrid nanostructured AFCNT-MoS₂ is further examined by GCD at different current densities at 0.5, 1, 2, and 5 A g⁻¹, as shown in Figure 6b. The nonlinear charge–discharge profiles show the pseudonature of MoS₂ in the hybrid. The stability of the capacitance is further evaluated by plotting between specific capacitance and current density, as shown in Figure 6c. The specific capacitance obtained from charge–discharge of the AFCNT-MoS₂ hybrid was found to be 516, 448, 370, and 291 F g⁻¹, corresponding to the current densities of 0.5, 1, 2, and 5 A g⁻¹, respectively, as shown in Figure 6c. The aforementioned analyses show that the hybrid material retained its specific capacitance even at higher current densities, showing that the material had not developed any resistance and confirming the good interconnection between AFCNT and MoS₂.

The electrochemical impedance analysis was done to evaluate the ESR in both cases, before and after testing the 5000 number of cycles. It was observed from **Figure 7**a that cell had not developed much of ESR even after 5000 cycles. It was also seen that the slope of the Nyquist plot slightly deviates from the negative imaginary axis, indicating that the cell retained good capacitance limited by diffusion resistance. To quantitatively determine the value of charge transfer resistance (R_{ct}), EIS data of the AFCNT-MoS₂ hybrid were simulated using the equivalent circuit model, as shown in the inset of Figure 7a. In the presented equivalent circuit model, R_s represents bulk resistance of the electrochemical system, R_{ct} indicates charge transfer resistance, W is the Warburg impedance, C_{dl} indicates double-layer capacitance, and C_p represents pseudocapacitance. The values for R_s and R_{ct} were found to be $0.6466 \, \Omega$ and $84.93 \times 10^{-9} \, \Omega$ by fitting the equivalent circuit model. The fitted curve of EIS data before and after the cycle is shown in Figure S13, Supporting Information. The absence of the semicircle is a reflection of the electrode not developing charge transfer resistance unlike batteries, a prerequisite for the SC electrode.[75] Impedance parameters were derived from the equivalent circuit model for AFCNT-MoS₂ electrode, as shown in **Table 1**.
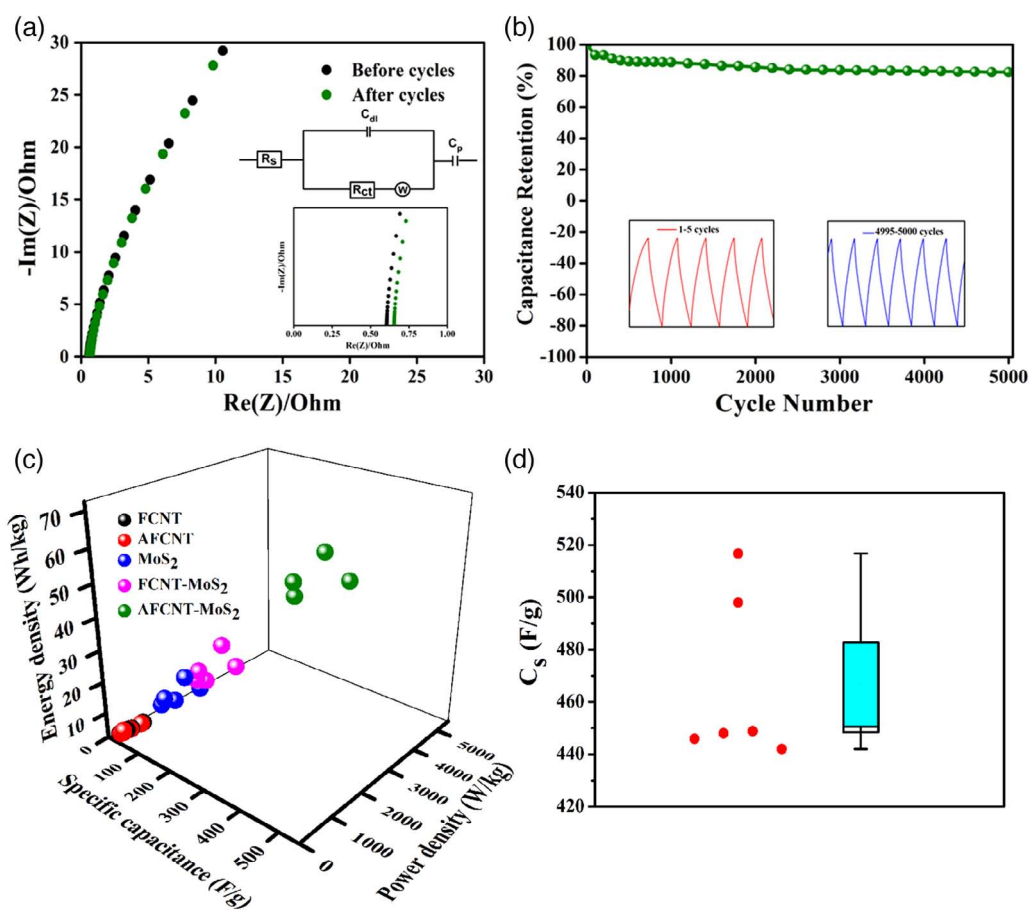

Figure 7. a) Nyquist plot of AFCNT-MoS₂, the inset shows the low-frequency region and equivalent circuit model. b) Degradation test of the AFCNT-MoS₂ electrode performed with 1000 charge/discharge cycles at 1 A g⁻¹, showing the degradation of electrode specific capacitance during the test, with (insets) plots of the first and last five charge/discharge cycles (time axes *t* is referenced to the beginning of each ten-cycle set). c) Measurement results and comparison of the energy density, power density, and capacitance of the FCNT, AFCNT, MoS₂, FCNT-MoS₂, and AFCNT-MoS₂ electrodes. d) Performance of several other devices in terms of specific capacitance.

Table 1. Impedance parameters derived using the equivalent circuit model for AFCNT-MoS$_2$ electrode.

Parameter	Value
R_s	$0.6466\,\Omega$
R_{ct}	$84.93 \times 10^{-9}\,\Omega$
C_{dl}	$2.787 \times 10^{-3}\,F$
C_p	$0.01308\,F$
W	$54.43\,\Omega\,s^{1/2}$

The cyclic performance of the hybrid material AFCNT-MoS$_2$ is shown in Figure 7b, which clearly shows that the cell retained 82.4% of the initial capacitance after 5000 cycles. The insets in Figure 7b show the first 5 (1–5) and the last 5 (4995–5000) cycles, to observe the charge discharge profile after running 5000 cycles. The charge–discharge profiles were observed to be linear and symmetric even in the last five cycles of 5000 cycles,

stating that the material had not developed any significant charge transfer resistance.

The structure stability of the AFCNT-MoS$_2$ electrodes was studied by checking morphologies before and after 5000 cycles and is shown in Figure S12a,b, Supporting Information, respectively. No significant changes in the morphology of AFCNT-MoS$_2$ hybrid was observed even after 5000 charge–discharge cycles, indicating good structural stability.

Figure 7c shows a 3D plot comparing the specific capacitance, energy density, and power density among the samples. It is shown that AFCNT-MoS$_2$ has the highest value among all the materials considered here with a specific capacitance of 516 F g^{-1}, energy density of 71.76 Wh kg^{-1}, and power density of 1000 W kg^{-1}. The comparison curve (Figure 5) shows the huge hike in the specific capacitance, energy density, and power density values for AFCNT-MoS$_2$, as compared with FCNT. This contrast between their performance values is possibly due to the high charge storage ability of MoS$_2$ with its layered structure, providing easy access for the ions of the electrolyte
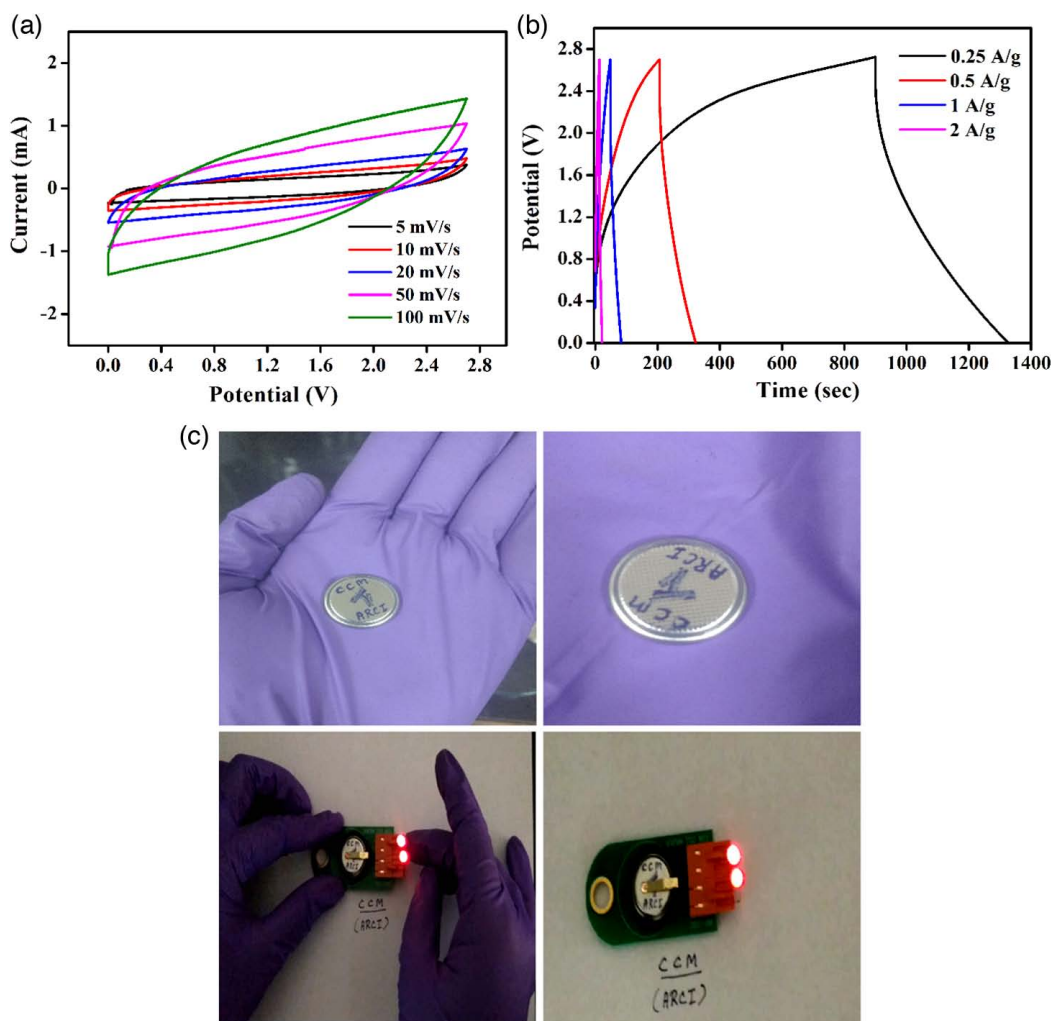

Figure 8. Electrochemical performances of AFCNT-MoS$_2$ hybrid nanostructured electrode with organic electrolyte in a two-electrode system for demonstrating the device functioning: a) CV curves at different scan rates of 5, 10, 20, 50, and 100 mV s^{-1}. b) Specific capacitance of AFCNT-MoS$_2$ at 0.5, 1, 2, and 5 scan rates. c) Photograph demonstrating the powering of red LEDs with coin cell-type SC device fabricated from AFCNT-MoS$_2$ hybrid.

to intercalate and deintercalate and their reduced interfacial resistance after the hybrid formation with activated FCNT. The performance distribution of several SC devices (Figure 7d) has been made using AFCNT-MoS$_2$ hybrid as an electrode material. It was found that the hybrid material AFCNT-MoS$_2$ showed excellent performance, each time showing a high specific capacitance value in the range of 450–520 F g^{-1}. Thus, AFCNT-MoS$_2$ has the ability to be a good SC electrode material in high energy-density applications.

To assess its practical application ability, the hybrid nanostructured electrode material of AFCNT-MoS$_2$ was tested with an organic electrolyte. The organic electrolyte is commercially used as it provides a wider potential window (2.7 V), leading to a high energy density. In this work, AFCNT-MoS$_2$ was used in a full-cell system, using CR2032 coin cell with 1 M TEABF$_4$ in acetonitrile electrolyte with the polypropylene (Ppy) separator. The coin cell of AFCNT-MoS$_2$ was fabricated inside a glovebox in inert argon atmosphere. The electrochemical analysis was done with a potential window of 2.7 V. The CV analysis with perfectly quasirectangular curves shown in **Figure 8**a,b shows the charge–discharge profiles obtained from the GCD analysis, which were slightly nonlinear but still symmetric at high current densities. The cell was tested for its practical ability by glowing LEDs, as shown in Figure 8c. It was observed that charging the cell for 2 min resulted in a constant glow of the LED for 4–5 min during its discharge phase after which the LED starts dimming out due to its cut-off potential. This shows that AFCNT-MoS$_2$ has the ability for practical applications.

3. Conclusions

The hybrid nanostructured material of AFCNT-MoS$_2$ was synthesized using a facile hydrothermal technique. The electrochemical performance of the AFCNT-MoS$_2$ hybrid electrode resulted in an excellent specific capacitance of 516 F g^{-1} at a current density of 0.5 A g^{-1} with an enhanced energy and power density of 71.76 Wh kg^{-1} and 1000 W g^{-1}. AFCNT-MoS$_2$ hybrid resulted in a minimal charge transfer resistance (ESR) value of 0.652 Ω and a high capacitance retention of 82.4% even after 5000 repeated cycles. The growth of MoS$_2$ nanoflowers on the surface of activated functionalized CNTs resulted in an encouraging charge storage ability and improved power and energy density. The structural features of AFCNT and MoS$_2$ were retained in the hybrid, as shown in the XRD and Raman analyses. The functional groups on the surface of CNTs were successfully attached and characterized using the FTIR. The microstructural studies obtained from FESEM and TEM support the argument of the overall improved performance by the ability of MoS$_2$ nanoflowers' high storage, whereas the well-bonded AFCNT acts as the electron transporting path. The specific surface area of AFCNT was around 30 times of the CNT, which was a significant enhancement due to the incorporation of the activation step, and it eventually helped in achieving the high specific capacitance for the AFCNT-MoS$_2$ hybrid electrode-based SC. The potential of AFCNT-MoS$_2$ hybrid electrode material was further confirmed using organic electrolyte and glowing LEDs at a lab scale, which shows the applicability of this electrode material for commercial SC applications with a high performance and energy density

features. Due to the simplicity, the proposed synthesis process of AFCNT-MoS$_2$ hybrid electrode material can be scaled up easily to industrial scale, which will certainly help in making SC devices on a large scale with low costs. We strongly believe that AFCNT-MoS$_2$ hybrid has the potential to be used in the commercial level as an electrode material in high-performance SC devices in terms of high specific capacitance, energy, and power density.

4. Experimental Section

Materials: All the chemicals used in this experiment were of analytical grade and used without further purification. The precursors used were hydrochloric acid (HCl) (SDFC chemicals, 35.4% pure), nitric acid (HNO$_3$) (Fisher Scientific, 75% pure), cetyl trimethyl ammonium bromide (CTAB) (C$_{18}$H$_{42}$BrN) (SRL chemicals, 99% pure), ammonium molybdate [(NH$_4$)$_6$Mo$_7$O$_{24}$·4H$_2$O] (Fisher Scientific, 98% pure), and thiourea (H$_2$NCSNH$_2$) (EMPARTA ACS, 99% pure). The multiwalled CNTs used were grown using the catalyst-assisted chemical vapor deposition technique, and the diameters of CNTs were in the range of 15–25 nm.

Synthesis of Functionalized Carbon Nanotubes: In the first step, CNTs were oxidized at 350 °C for 1 h in air in a muffle furnace for removing any amorphous carbon, followed by the 31 wt% HCl treatment for 18 h for removing the metal catalyst in the CNT; it was then washed thoroughly with deionized (DI) water to maintain the pH level 7 and finally vacuum filtered. Afterward, the resultant product was refluxed at 180 °C for 4 h in the presence of 10 M HNO$_3$ to generate functional groups in the surface of CNTs. The functional groups such as —OH, —C—O, and C=C were determined from FTIR analysis (Figure S3, Supporting Information) and the detailed analysis is given in "Results" section. The functionalized CNTs were carefully washed with DI water, until the pH level reached 7, and collected using vacuum filtration. The obtained product was dried overnight in a vacuum oven at 120 °C.[67]

Synthesis of Activated Functionalized Carbon Nanotubes: First, FCNTs and KOH flakes (weight ratio 1:2.2) were mixed to form a powder-like mixture. Then the mixture was transferred into the muffle furnace in nitrogen atmosphere. Initially, the temperature was raised to 120 °C with a heating rate of 5 °C min^{-1} and held at this temperature for 30 min to remove the moisture accumulated during mixing due to the hygroscopic nature of KOH. Later, the temperature was raised to 750 °C with the same heating rate and held at this temperature for 120 min. The furnace was allowed to cool down naturally after the activation process.

The sample was collected after activation and thoroughly washed with DI water to remove any traces of KOH left in the mixture. Later the mixture was vacuum filtered to bring the pH to 7. The neutralized wet mixture was then treated with 0.1 M HCl for 30 min by means of stirring to remove the intercalated K traces from the activated mixture. Finally, the mixture was again vacuum filtered to bring back the pH to 7 and dried in a vacuum oven at 120 °C for 16 h, and it was followed by hydrogen annealing. Hydrogen annealing was done at 900 °C for 2 h, and the flow rate was maintained at 50 SCCM. The resulting powder is encoded as AFCNT.[52,68–70]

Synthesis of Molybdenum Sulfide: MoS$_2$ was prepared using the simple one-step hydrothermal method.[56] In the process, ammonium molybdate and thiourea in the weight ratio of 3:4 were dissolved in the 50 mL DI water by magnetic stirring for 1 h. Subsequently, the mixture was transferred into a 125 mL Teflon-lined stainless-steel autoclave and heated at 220 °C for 24 h. After cooling naturally, the black precipitate was collected by vacuum filtration and washed with distilled water several times to adjust the pH level to neutral (pH = 7) and dried in a vacuum oven overnight.

Synthesis of FCNT-MoS$_2$ Hybrid: The FCNT-MoS$_2$ nanoflowers were synthesized using the hydrothermal synthesis route.[76] First of all, the as-prepared 40 mg of functionalized CNTs were mixed into 50 mL CTAB solution (maintaining the critical micelle concentration [CMC]) under constant stirring, followed by ultrasonication for 1 h for homogeneous mixing at room temperature. Soon after, 151 mg ammonium molybdate and 200 mg thiourea were added into the above as-prepared solution and ultrasonicated for 30 min. The homogeneous solution was

then transferred into the 125 mL Teflon-lined autoclave and heat treated at 220 °C for 24 h. The as-obtained dark suspension was washed with the DI water several times until the pH level became 7 and vacuum filtered. Finally, the as-obtained powder was kept in a vacuum oven for drying at 120 °C overnight.

Synthesis of AFCNT-MoS$_2$ Hybrid: For synthesizing AFCNT-MoS$_2$, the same procedure was used as FCNT-MoS$_2$. Only the AFCNTs were used at the place of FCNTs.

Characterization: The crystallographic studies were conducted using XRD (model: Bruker D8 Advance, Cu Kα [$\lambda = 1.54$ °A] source, scan rate of 1.20 min^{-1}) in the reflection mode. For the analysis, the sample was well grounded with a mortar–pestle to obtain a fine powder for XRD analysis.

The morphological characterization of hybrid materials was conducted with FESEM (ZEISS Gemini SEM-500), operated at 5 kV. The sample for the FESEM analysis was prepared by taking a pinch of the finely powdered sample on the carbon tape.

The microstructural analysis of the prepared nanostructures was conducted using TEM (model: TECNAI G^2). For the analysis, the AFCNT-MoS$_2$ hybrid sample was dispersed in ethanol using ultrasonication to obtain a homogeneous suspension. Later, one drop of the solution was dropped on to a holy carbon-coated Cu grid of 300 mesh and later dried overnight before TEM characterization.

FTIR (BRUKER) was used to investigate the presence of functional groups in FCNTs. The sample for the analysis was prepared using 1:200 (weight ratio) of FCNT:KBr for making a transparent pellet.

RAMAN (Witech-alpha 300) was used to record the Raman spectrum using the laser of the excitation wavelength 532 nm.

The chemical compositional analysis was conducted by XPS using an X-ray source (Al = 1486 eV) and the Kratos Axis Ultra DLD spectrometer. The X-ray spot size was 400 µm^2 with a penetration depth of ≈10 nm. The sample analysis chamber pressure was maintained at 10^{-9} bar for all measurements. Current and voltage were 10 mA and 15 kV, respectively, during the measurements. The samples were dispersed in ethanol without further purification and were spray coated onto the Si (N type, 100) substrate for XPS analysis. Specific region scans were conducted at a resolution of 0.05 eV and pass energy of 20 eV. Calibration was conducted using the C 1s peak located at 284.5 eV.

The specific surface area was obtained by the low-temperature nitrogen adsorption–desorption analysis via a surface analyzer (Micromeritics ASAP 2020, V3.00 H). Samples were outgassed overnight at a temperature of 250 °C to remove the surface impurities such as the adsorbed moisture, and the adsorption–desorption process was conducted against a relative pressure at 77 K. The specific surface area was calculated using the BET method.

The electrochemical properties were characterized with GCD, CV, and EIS techniques, at room temperature, using the CHI-600D electrochemical workstation.

The electrochemical test was conducted using the two-electrode configuration in a swagelok cell shown in Figure S10, Supporting Information. The working electrodes were fabricated using 80 wt% of the as-synthesized material as an active material with 10 wt% of PVDF as the binder and 10 wt% of carbon black, respectively. The mixture was ground using a mortar and pestle. Later, the mixture was made into a slurry using *N*-methyl 2-pyrollidone (NMP). The mixed slurry was coated on to the exfoliated graphite sheet, of thickness 350 µm, to make electrodes, and it was kept in a vacuum oven for overnight drying at 120 °C. The two-electrode cell configuration was arranged using a swagelok cell. The cell consisted of two electrodes separated by a Whatman separator wetted with 3 M KOH electrolyte.

The specific capacitance from CV, specific capacitance from GCD, power density, and energy density values were calculated using the formulas given in Supporting Information (S5) and the parameters used are given in detail in Supporting Information (S4).

Supporting Information

Supporting Information is available from the Wiley Online Library or from the author.

Conflict of Interest

The authors declare no conflict of interest.

[1] J. Chow, R. J. Kopp, P. R. Portney, *Science* **2003**, *302*, 1528.

[2] D. P. Dubal, R. Holze, *Energy* **2013**, *51*, 407.

[3] A. González, E. Goikolea, J. A. Barrena, R. Mysyk, *Renewable Sustainable Energy Rev.* **2016**, *58*, 1189.

[4] K. Gopalakrishnan, S. Sultan, A. Govindaraj, C. N. R. Rao, *Nano Energy* **2015**, *12*, 52.

[5] P. B. Karandikar, D. B. Talange, U. P. Mhaskar, R. Bansal, *Energy* **2012**, *40*, 131.

[6] B. Kim, H. Chung, W. Kim, *Nanotechnology* **2012**, *23*, 155401.

[7] W.-Y. Ko, Y.-F. Chen, K.-M. Lu, K.-J. Lin, *Sci. Rep.* **2016**, *6*, 18887.

[8] L. Li, Z. Wu, S. Yuan, X.-B. Zhang, *Energy Environ. Sci.* **2014**, *7*, 2101.

[9] Z. Li, Z. Qin, B. Yang, J. Guo, H. Wang, W. Zhang, X. Lv, A. Stack, *Nanotechnology* **2015**, *26*, 065401.

[10] D. Qi, Y. Liu, Z. Liu, L. Zhang, X. Chen, *Adv. Mater.* **2017**, *29*, 1602802.

[11] X. Dong, N. Hu, L. Wei, Y. Su, H. Wei, L. Yao, X. Li, Y. Zhang, *J. Mater. Chem. A* **2016**, *4*, 9739.

[12] Z. Li, Z. Zhou, G. Yun, K. Shi, X. Lv, B. Yang, *Nanoscale Res. Lett.* **2013**, *8*, 473.

[13] Y. Shao, M. F. El-Kady, L. J. Wang, Q. Zhang, Y. Li, H. Wang, M. F. Mousavi, R. B. Kaner *Chem. Soc. Rev.* **2015**, *44*, 3639.

[14] J. Gamby, P. L. Taberna, P. Simon, J. F. Fauvarque, M. Chesneau, *J. Power Sources* **2001**, *101*, 109.

[15] Y. Wang, Z. Shi, Y. Huang, Y. Ma, C. Wang, M. Chen, Y. Chen, *J. Phys. Chem. C* **2009**, *113*, 13103.

[16] C. Liu, Z. Yu, D. Neff, A. Zhamu, B. Z. Jang, *Nano Lett.* **2010**, *10*, 4863.

[17] E. Frackowiak, K. Metenier, V. Bertagna, F. Beguin, *Appl. Phys. Lett.* **2000**, *77*, 2421.

[18] Y. Hou, Y. Cheng, T. Hobson, J. Liu, *Nano Lett.* **2010**, *10*, 2727.

[19] H. Jiang, J. Ma, C. Li, *Adv. Mater.* **2012**, *24*, 4197.

[20] H. Jiang, T. Zhao, C. Li, J. Ma, *J. Mater. Chem.* **2011**, *21*, 3818.

[21] R. R. Salunkhe, K. Jang, S.-W. Lee, S. Yu, H. Ahn, *J. Mater. Chem.* **2012**, *22*, 21630.

[22] S. Ratha, C. S. Rout, *ACS Appl. Mater. Interfaces* **2013**, *5*, 11427.

[23] M. Acerce, D. Voiry, M. Chhowalla, *Nat. Nanotechnol.* **2015**, *10*, 313.

[24] K.-J. Huang, L. Wang, J.-Z. Zhang, L.-L. Wang, Y.-P. Mo, *Energy* **2014**, *67*, 234.

[25] J. Yan, *Handbook of Clean Energy Systems*, John Wiley & Sons, Chichester **2015**.

[26] A. Young Rack, S. Mi Yeon, J. Seong Mu, P. Chong Rae, K. Dong Young, *Nanotechnology* **2006**, *17*, 2865.

[27] V. D. Patake, C. D. Lokhande, O. S. Joo, *Appl Surf. Sci.* **2009**, *255*, 4192.

[28] C.-C. Hu, Y.-H. Huang, K.-H. Chang, *J. Power Sources* **2002**, *108*, 117.

[29] J. Yan, T. Wei, J. Cheng, Z. Fan, M. Zhang, *Mater. Res. Bull.* **2010**, *45*, 210.

[30] P. A. Nelson, J. R. Owen, *J. Electrochem. Soc.* **2003**, *150*, A1313.

[31] U. M. Patil, R. R. Salunkhe, K. V. Gurav, C. D. Lokhande, *Appl. Surf. Sci.* **2008**, *255*, 2603.

[32] S. G. Kandalkar, J. L. Gunjakar, C. D. Lokhande, *Appl. Surf. Sci.* **2008**, *254*, 5540.

[33] N. Miura, S. Oonishi, K. R. Prasad, *Electrochem. Solid-State Lett.* **2004**, *7*, A247.

[34] C.-C. Hu, C.-M. Huang, K.-H. Chang, *J. Power Sources* **2008**, *185*, 1594.

[35] M. Nakayama, A. Tanaka, Y. Sato, T. Tonosaki, K. Ogura, *Langmuir* **2005**, *21*, 5907.

[36] G. Wang, L. Zhang, J. Zhang, *Chem. Soc. Rev.* **2012**, *41*, 797.

[37] Z.-S. Wu, D.-W. Wang, W. Ren, J. Zhao, G. Zhou, F. Li, H.-M. Cheng, *Adv. Funct. Mater.* **2010**, *20*, 3595.

[38] A. Ferris, S. Garbarino, D. Guay, D. Pech, *Adv. Mater.* **2015**, *27*, 6625.

[39] M. Chhowalla, G. A. J. Amaratunga, *Nature* **2000**, *407*, 164.

[40] K. J. Huang, L. Wang, J. Li, Y.-M. Liu, *Sens. Actuator B-Chem.* **2013**, *178*, 671.

[41] K.-J. Huang, L. Wang, Y.-J. Liu, T. Gan, Y.-M. Liu, L.-L. Wang, Y. Fan, *Electrochim. Acta* **2013**, *107*, 379.

[42] H. S. S. Ramakrishna Matte, A. Gomathi, A. K. Manna, D. J. Late, R. Datta, S. K. Pati, C. N. R. Rao, *Angew. Chem.* **2010**, *49*, 4059.

[43] R. R. Haering, J. A. Stiles, K. Brandt, *Google Patents* US4224390A, **1980**.

[44] N. Zheng, X. Bu, P. Feng, *Nature* **2003**, *426*, 428.

[45] D. Kong, H. He, Q. Song, B. Wang, W. Lv, Q.-H. Yang, L. Zhi, *Energy Environ. Sci.* **2014**, *7*, 3320.

[46] J. M. Soon, K. P. Loh, *Electrochem. Solid-State Lett.* **2007**, *10*, A250.

[47] K.-J. Huang, L. Wang, Y.-J. Liu, Y.-M. Liu, H.-B. Wang, T. Gan, L.-L. Wang, *Int. J. Hydrogen Energy* **2013**, *38*, 14027.

[48] A. Ramadoss, T. Kim, G.-S. Kim, S. J. Kim, *New J. Chem.* **2014**, *38*, 2379.

[49] E. G. da Silveira Firmiano, A. C. Rabelo, C. J. Dalmaschio, A. N. Pinheiro, E. C. Pereira, W. H. Schreiner, E. R. Leite, *Adv. Energy Mater.* **2014**, *4*, 1301380.

[50] Y. Yang, H. Fei, G. Ruan, C. Xiang, J. M. Tour, *Adv. Mater.* **2014**, *26*, 8163.

[51] S. Zhang, B. V. R. Chowdari, Z. Wen, J. Jin, J. Yang, *ACS Nano* **2015**, *9*, 12464.

[52] E. Raymundo-Pinero, P. Azais, T. Cacciaguerra, D. Cazorla-Amorós, A. Linares-Solano, F. Béguin, *Carbon* **2005**, *43*, 786.

[53] G. Huang, T. Chen, W. Chen, Z. Wang, K. Chang, L. Ma, F. Huang, D. Chen, J. Y. Lee, *Small* **2013**, *9*, 3693.

[54] S. Costa, E. Borowiak-Palen, M. Kruszynska, A. Bachmatiuk, R. Kalenczuk, *Mater. Sci-Poland* **2008**, *26*, 433.

[55] S. Kamila, B. Mohanty, A. K. Samantara, P. Guha, A. Ghosh, B. Jena, P. V. Satyam, B. Mishra, B. K. Jena, *Sci. Rep.* **2017**, *7*, 8378.

[56] K. Gopalakrishnan, K. Pramoda, U. Maitra, U. Mahima, M. Shah, C. Rao, *Nanomater. Energy* **2015**, *4*, 9.

[57] A. Osorio, I. Silveira, V. Bueno, C. Bergmann, *Appl. Surf. Sci.* **2008**, *255*, 2485.

[58] Y. Yan, X. Ge, Z. Liu, J.-Y. Wang, J.-M. Lee, X. Wang, *Nanoscale* **2013**, *5*, 7768.

[59] Y. Shi, Y. Wang, J. I. Wong, A. Y. S. Tan, C.-L. Hsu, L.-J. Li, Y.-C. Lu, H. Y. Yang, *Sci. Rep.* **2013**, *3*, 2169.

[60] H. Huang, W. Huang, Z. Yang, J. Huang, J. Lin, W. Liu, Y. Liu, *J. Mater. Chem.* **2017**, *5*, 1558.

[61] V. O. Koroteev, L. G. Bulusheva, I. P. Asanov, E. V. Shlyakhova, D. V. Vyalikh, A. V. Okotrub, *J. Phys. Chem. C* **2011**, *115*, 21199.

[62] V. Koroteev, L. Bulusheva, I. Asanov, E. Shlyakhova, D. Vyalikh, A. Okotrub, *J. Phys. Chem. C* **2011**, *115*, 21199.

[63] T. Weber, J. Muijsers, J. Van Wolput, C. Verhagen, J. Niemantsverdriet, *J. Phys. Chem. C* **1996**, *100*, 14144.

[64] H. W. Wang, P. Skeldon, G. E. Thompson, *Surf. Coat. Tech.* **1997**, *91*, 200.

[65] N. H. Tran, M. A. Wilson, A. S. Milev, J. R. Bartlett, R. N. Lamb, D. Martin, G. S. K. Kannangara, *Adv. Colloid Interface Sci.* **2009**, *145*, 23.

[66] X. C. Song, Y. F. Zheng, Y. Zhao, H. Y. Yin, *Mater. Lett* **2006**, *60*, 2346.

[67] Z. Liu, J. Wang, V. Kushvaha, S. Poyraz, H. Tippur, S. Park, M. Kim, Y. Liu, J. Bar, H. Chen, X. Zhang, *Chem. Commun.* **2011**, *47*, 9912.

[68] L. Donnaperna, L. Duclaux, R. Gadiou, Y. Soneda, N. Yoshizawa, *Carbon – Sci. Technol.* **2009**, *3*, 120.

[69] J. Wang, S. Kaskel, *J. Mater. Chem.* **2012**, *22*, 23710.

[70] C. He, S. Song, J. Liu, V. Maragou, P. Tsiakaras, *J. Power Sources* **2010**, *195*, 7409.

[71] Y. Wang, Y. Song, Y. Xia, *Chem. Soc. Rev.* **2016**, *45*, 5925.

[72] D. Yu, L. Dai, *J. Phys. Chem. Lett.* **2009**, *1*, 467.

[73] A. Laheäär, P. Przygocki, Q. Abbas, F. Béguin, *Electrochem. Commun.* **2015**, *60*, 21.

[74] Z. Li, Y. Zhang, W. Zhang, *Mater. Res. Express* **2017**, *4*, 055018.

[75] F. Pan, J. Wang, Z. Yang, L. Gu, Y. Yu, *RSC Adv.* **2015**, *5*, 77518.

[76] J. Li, Y. Hou, X. Gao, D. Guan, Y. Xie, J. Chen, C. Yuan, *Nano Energy* **2015**, *16*, 10.